Monthly Notices
of the
ROYAL ASTRONOMICAL SOCIETY

MNRAS **496,** 1638–1644 (2020)
Advance Access publication 2020 June 10

doi:10.1093/mnras/staa1628

Confirmation of water emission in the dayside spectrum of the ultrahot Jupiter WASP-121b

Thomas Mikal-Evans [1]★ David K. Sing,[2,3] Tiffany Kataria,[4] Hannah R. Wakeford [5] Nathan J. Mayne,[6] Nikole K. Lewis,[7] Joanna K. Barstow[8] and Jessica J. Spake [2]

[1]*Kavli Institute for Astrophysics and Space Research, Massachusetts Institute of Technology, 77 Massachusetts Avenue, 37-241, Cambridge, MA 02139, USA*
[2]*Department of Earth & Planetary Sciences, Johns Hopkins University, Baltimore, MD 21210, USA*
[3]*Department of Physics & Astronomy, Johns Hopkins University, Baltimore, MD 21210, USA*
[4]*NASA Jet Propulsion Laboratory, 4800 Oak Grove Drive, Pasadena, CA 91109, USA*
[5]*School of Physics, University of Bristol, HH Wills Physics Laboratory, Tyndall Avenue, Bristol BS8 1TL, UK*
[6]*Astrophysics Group, University of Exeter, Exeter EX4 2QL, UK*
[7]*Department of Astronomy and Carl Sagan Institute, Cornell University, 122 Sciences Drive, Ithaca, NY 14853, USA*
[8]*Department of Physics and Astronomy, University College London, Gower Street, London WC1E 6BT, UK*

Accepted 2020 May 17. Received 2020 April 30; in original form 2020 February 28

ABSTRACT

We present four new secondary eclipse observations for the ultrahot Jupiter WASP-121b acquired using the *Hubble Space Telescope* Wide Field Camera 3. The eclipse depth is measured to a median precision of 60 ppm across 28 spectroscopic channels spanning the 1.12–1.64 μm wavelength range. This is a considerable improvement to the 90 ppm precision we achieved previously for a single eclipse observation using the same observing set-up. Combining these data with those reported at other wavelengths, a blackbody spectrum for WASP-121b is ruled out at $>6\sigma$ confidence and we confirm the interpretation of previous retrieval analyses that found the data are best explained by a dayside thermal inversion. The updated spectrum clearly resolves the water emission band at 1.3–1.6 μm, with higher signal-to-noise than before. It also fails to reproduce a bump in the spectrum at 1.25 μm derived from the first eclipse observation, which had tentatively been attributed to VO emission. We conclude that the latter was either a statistical fluctuation or a systematic artefact specific to the first eclipse data set.

Key words: techniques: spectroscopic – planets and satellites: atmospheres.

1 INTRODUCTION

In the case of a synchronously orbiting, highly irradiated planet, if the opacity of the atmosphere is lower at optical wavelengths than at infrared wavelengths, the vertical temperature profile of the dayside hemisphere is expected to decrease with decreasing pressure close to the infrared photosphere. This is essentially because most of the incident stellar radiation is at optical wavelengths. Therefore, if the optical opacity of the atmosphere is lower than the infrared opacity, the stellar radiation will be primarily deposited below the infrared photosphere, heating the atmosphere at those higher pressures. Conversely, if the optical opacity is higher than the infrared opacity, most of the heating by the host star will occur above the infrared photosphere, resulting in a thermal inversion. As such, thermal inversions are valuable diagnostics of the radiative processes at play in a planetary atmosphere, and in particular, the relative strength of absorption at optical versus infrared wavelengths.

Observationally, thermal inversions can be inferred by measuring the planetary emission spectrum and detecting opacity bands as emission rather than absorption features. The first detection of a spectrally resolved emission feature for an exoplanet was made by Evans et al. (2017) for WASP-121b, an ultrahot Jupiter discovered by Delrez et al. (2016). This was done by observing a secondary eclipse with the *Hubble Space Telescope* (*HST*) Wide Field Imaging Camera 3 (WFC3). The resulting dayside spectrum derived from these data revealed an H_2O emission band spanning the ∼1.3–1.6 μm wavelength range, providing strong evidence for a dayside thermal inversion (Evans et al. 2017). Additional observations made with the *Spitzer Space Telescope* (Garhart et al. 2020), ground-based photometry (Delrez et al. 2016; Kovács & Kovács 2019), *HST* (Mikal-Evans et al. 2019), and the *Transiting Exoplanet Survey Satellite* (*TESS*; Bourrier et al. 2020a; Daylan et al. 2019) have since extended the wavelength coverage of the WASP-121b emission

★ E-mail: tmevans@mit.edu

spectrum considerably. In addition to the H_2O emission band, this combined data set shows evidence for H^- and CO emission, with retrieval analyses inferring a temperature profile that increases from ∼2500 to ∼2800 K across the ∼30–5 mbar pressure range (Mikal-Evans et al. 2019).

It has not yet been possible to identify optical opacity source(s) in the dayside atmosphere of WASP-121b and definitively link them to the thermal inversion. Early studies focused on the strong optical absorbers TiO and VO as likely candidates for generating thermal inversions in highly irradiated atmospheres, in which the temperatures are high enough (≳2000 K) for these species to be in the gas phase (Hubeny, Burrows & Sudarsky 2003; Fortney et al. 2008). Indeed, evidence for VO absorption has been uncovered in the transmission spectrum of WASP-121b, but not TiO (Evans et al. 2018; Merritt et al. 2020). However, recent theoretical work has highlighted that for ultrahot Jupiters with temperatures of ≳2700 K such as WASP-121b, much of the TiO and VO will likely be thermally dissociated on the dayside hemisphere, reducing their potency as thermal inversion drivers (Lothringer, Barman & Koskinen 2018; Parmentier et al. 2018). Instead, for these hottest planets, thermal inversions may be generated by heavy metals in the gas phase, such as Fe and Mg, which have strong absorption lines in the near-ultraviolet and optical (Lothringer et al. 2018). Statistically significant detections of Fe I, Fe II, and Mg II have been made in the transmission spectrum of WASP-121b (Sing et al. 2019; Bourrier et al. 2020b; Cabot et al. 2020; Gibson et al. 2020), supporting this hypothesis. Other near-ultraviolet/optical absorbers such as NaH, MgH, FeH, SiO, AlO, and CaO have also been suggested (Lothringer et al. 2018; Parmentier et al. 2018; Gandhi & Madhusudhan 2019), but no evidence has been uncovered for their presence in the atmosphere of WASP-121b to date.

This paper presents follow-up secondary eclipse observations for WASP-121b made with *HST* WFC3 that allow us to refine the dayside emission spectrum across the 1.12–1.64 μm wavelength range. In Section 2, we describe the observations and data reduction procedures, followed by the light-curve fitting methodology in Section 3. We discuss the results in Section 4 and give our conclusions in Section 5.

2 OBSERVATIONS AND DATA REDUCTION

Two full-orbit phase curves of WASP-121b were observed with *HST*/WFC3 on 2018 March 12–13 and 2019 February 3–4 (G.O. 15134; P.I.s: Mikal-Evans and Kataria). For both visits, the target was observed for approximately 40.3 h over 26 contiguous *HST* orbits. Each visit was scheduled to include two consecutive secondary eclipses. Here, we present an analysis of the four secondary eclipses acquired in this manner. The full phase curve will be presented in a future publication (Mikal-Evans et al., in preparation).

A similar observing set-up to that used previously in Evans et al. (2016, 2017) was adopted. Observations for both visits used the G141 grism, which encompasses the 1.12–1.64 μm wavelength range with a spectral resolving power of $R \sim 130$ at $\lambda = 1.4$ μm. The forward spatial-scanning mode was used and only a 256 × 256 subarray was read out from the detector with the SPARS10 sampling sequence and 15 non-destructive reads per exposure (NSAMP = 15), corresponding to exposure times of 103 s. The only difference between Evans et al. (2016, 2017) and the current observing set-up was that a slower spatial scan rate of 0.073 arcsec s^{-1} was used, compared to 0.120 arcsec s^{-1} for the earlier observations. This resulted in shorter scans across approximately 60 pixel-rows of the cross-dispersion axis, leaving more space on the detector for background estimation. With this set-up, we obtained 15 exposures in the first *HST* orbit following acquisition and 16 exposures in each subsequent *HST* orbit. Typical peak frame counts were ∼37 000 electrons per pixel for both visits, which is within the recommended range derived from an ensemble analysis of WFC3 spatial-scan data spanning 8 yr (Stevenson & Fowler 2019).

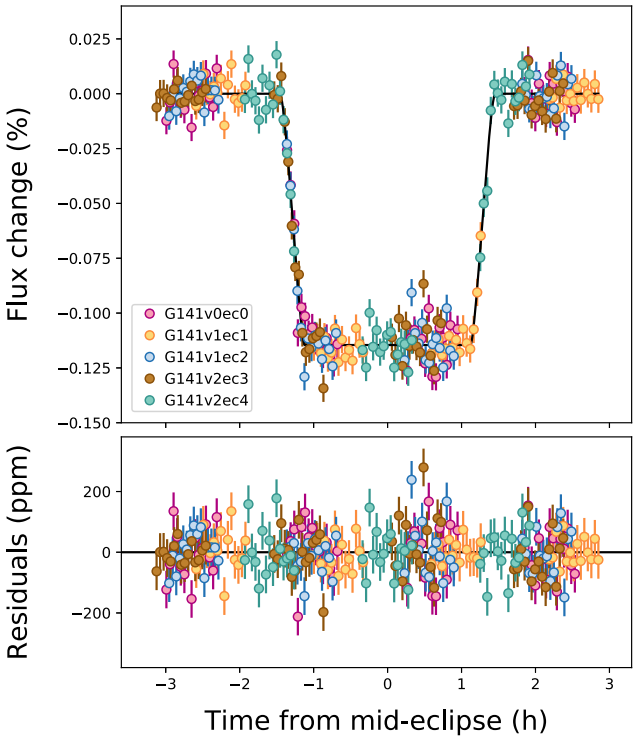

Figure 1. *(Top panel)* Phase-folded white light curve with eclipse model after removing systematics components of a joint fit to all five eclipses. *(Bottom panel)* Model residuals.

Spectra were extracted from the raw data frames using a custom-built PYTHON pipeline, which has been described previously (Evans et al. 2016, 2017; Mikal-Evans et al. 2019) and is similar to others employed in the field (e.g. Knutson et al. 2014; Kreidberg et al. 2014; Wakeford et al. 2017, 2018; Nikolov et al. 2018a). For each exposure, we took the difference between successive non-destructive reads and applied a 50-pixel-wide top-hat filter along the cross-dispersion axis, before summing to produce final reconstructed images. The top-hat filter applied in this way has the effect of removing contamination from nearby sources and most cosmic ray strikes on the detector. The target spectrum was then extracted from each image by integrating the flux within a rectangular aperture spanning the full dispersion axis and 100 pixels along the cross-dispersion axis, centred on the central cross-dispersion row of the scan. Background fluxes were assumed to be wavelength independent and subtracted from each spectrum. These were estimated by taking the median pixel count within a 10 × 170 pixel box located away from the target spectrum on the 2D reconstructed image, with typical background levels integrated over the full 103 s exposures starting at ∼150 electrons $pixel^{-1}$ and dropping to ∼110 electrons $pixel^{-1}$ over each *HST* orbit. The wavelength solution was determined by cross-correlating the final spectrum of each visit against a model stellar spectrum, as described in Evans et al. (2016).

Table 1. MCMC results for the joint fit to all five eclipse white light curves. Quoted values are the posterior medians and uncertainties give the ±34 per cent credible intervals about the median.

Parameter	Data set	Value
Eclipse depth (ppm)	All	1150^{+21}_{-19}
$T_{\rm mid}$ (MJD$_{\rm UTC}$)	G141v0ec0	$2457703.45707^{+0.00077}_{-0.00081}$
	G141v1ec1	$2458190.47621^{+0.00142}_{-0.00115}$
	G141v1ec2	$2458191.75090^{+0.00049}_{-0.00055}$
	G141v2ec3	$2458518.13064^{+0.00073}_{-0.00073}$
	G141v2ec4	$2458519.40663^{+0.00058}_{-0.00056}$

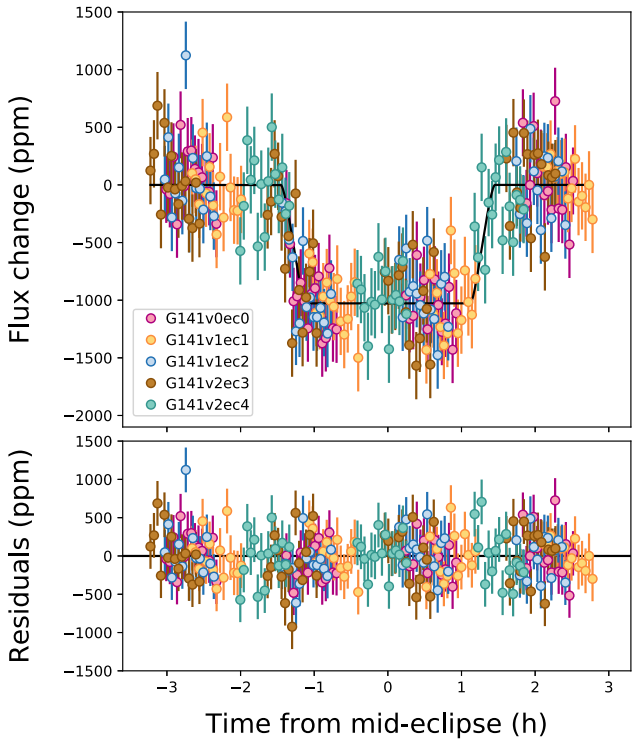

Figure 2. The same as Fig. 1, but for an example spectroscopic light curve spanning 1.231–1.249 μm in wavelength.

3 LIGHT-CURVE FITTING

White light curves were produced by summing the flux of each spectrum across the full wavelength range. We then fit the resulting light curves using the methodology described in Mikal-Evans et al. (2019), using a Gaussian process model to account for instrumental systematics. In addition to the four new eclipses presented in this study, we also analysed an eclipse acquired as part of an earlier *HST* programme (GO-14767; P.I.s: Sing and Lopez-Morales) that was originally published in Evans et al. (2017). We refer to the latter eclipse as G141v0ec0, the two eclipses observed as part of the 2018 visit as G141v1ec1 and G141v1ec2, and the two eclipses observed as part of the 2019 visit as G141v2ec3 and G141v2ec4. All five eclipses were fitted simultaneously, with separate systematics models and eclipse mid-times ($T_{\rm mid}$) for each data set, and a shared eclipse depth. We set the orbital period equal to 1.274 924 7646 d (Sing et al. 2019), and the normalized semimajor axis ($a/R_\star$) and impact parameter (b) were fixed to the same values adopted in Mikal-Evans et al. (2019), namely $a/R_\star = 3.86$ and $b = 0.06$. The resulting light-curve fit is shown in Fig. 1 and the inferred eclipse parameters are reported in Table 1.

Next, we generated spectroscopic light curves in 28 wavelength channels, using the method described in Mikal-Evans et al. (2019). Each of these light curves was then fitted with the same method used for the white light-curve fit, but with the eclipse mid-times held fixed to the best-fitting values obtained from the latter. An example light-curve fit is shown in Fig. 2. For all data sets and spectroscopic light curves, the residual scatter was consistent with being photon noise limited. Inferred eclipse depths are reported in Table 2.

Table 2. Eclipse depths inferred for each spectroscopic channel, quoted as median and ±34 per cent credible intervals from the MCMC fits.

Wavelength (μm)	Eclipse depth (ppm)
1.120–1.138	903^{+53}_{-52}
1.138–1.157	991^{+59}_{-60}
1.157–1.175	1002^{+58}_{-56}
1.175–1.194	1029^{+50}_{-49}
1.194–1.212	1066^{+58}_{-58}
1.212–1.231	983^{+54}_{-57}
1.231–1.249	1031^{+48}_{-51}
1.249–1.268	1015^{+55}_{-50}
1.268–1.286	994^{+49}_{-48}
1.286–1.305	1028^{+55}_{-53}
1.305–1.323	1008^{+55}_{-60}
1.323–1.342	1077^{+55}_{-56}
1.342–1.360	1160^{+51}_{-52}
1.360–1.379	1110^{+61}_{-57}
1.379–1.397	1262^{+57}_{-59}
1.397–1.416	1360^{+57}_{-56}
1.416–1.434	1193^{+54}_{-56}
1.434–1.453	1304^{+51}_{-54}
1.453–1.471	1331^{+58}_{-63}
1.471–1.490	1342^{+57}_{-57}
1.490–1.508	1304^{+62}_{-60}
1.508–1.527	1276^{+62}_{-62}
1.527–1.545	1210^{+66}_{-65}
1.545–1.564	1307^{+62}_{-60}
1.564–1.582	1388^{+63}_{-66}
1.582–1.601	1299^{+69}_{-69}
1.601–1.619	1270^{+64}_{-63}
1.619–1.638	1286^{+68}_{-68}

4 DISCUSSION

The updated WASP-121b emission spectrum is shown in Fig. 3. The new G141 data are in good overall agreement with the original spectrum presented in Evans et al. (2017). However, unlike the Evans et al. (2017) spectrum, the revised G141 spectrum does not exhibit a bump at 1.25 μm, which our previous investigations had failed to replicate with physically plausible atmosphere models (Evans et al. 2017; Mikal-Evans et al. 2019). This suggests that the 1.25 μm bump was either a statistical fluctuation or a systematic artefact specific to the G141v0ec0 data set, demonstrating the

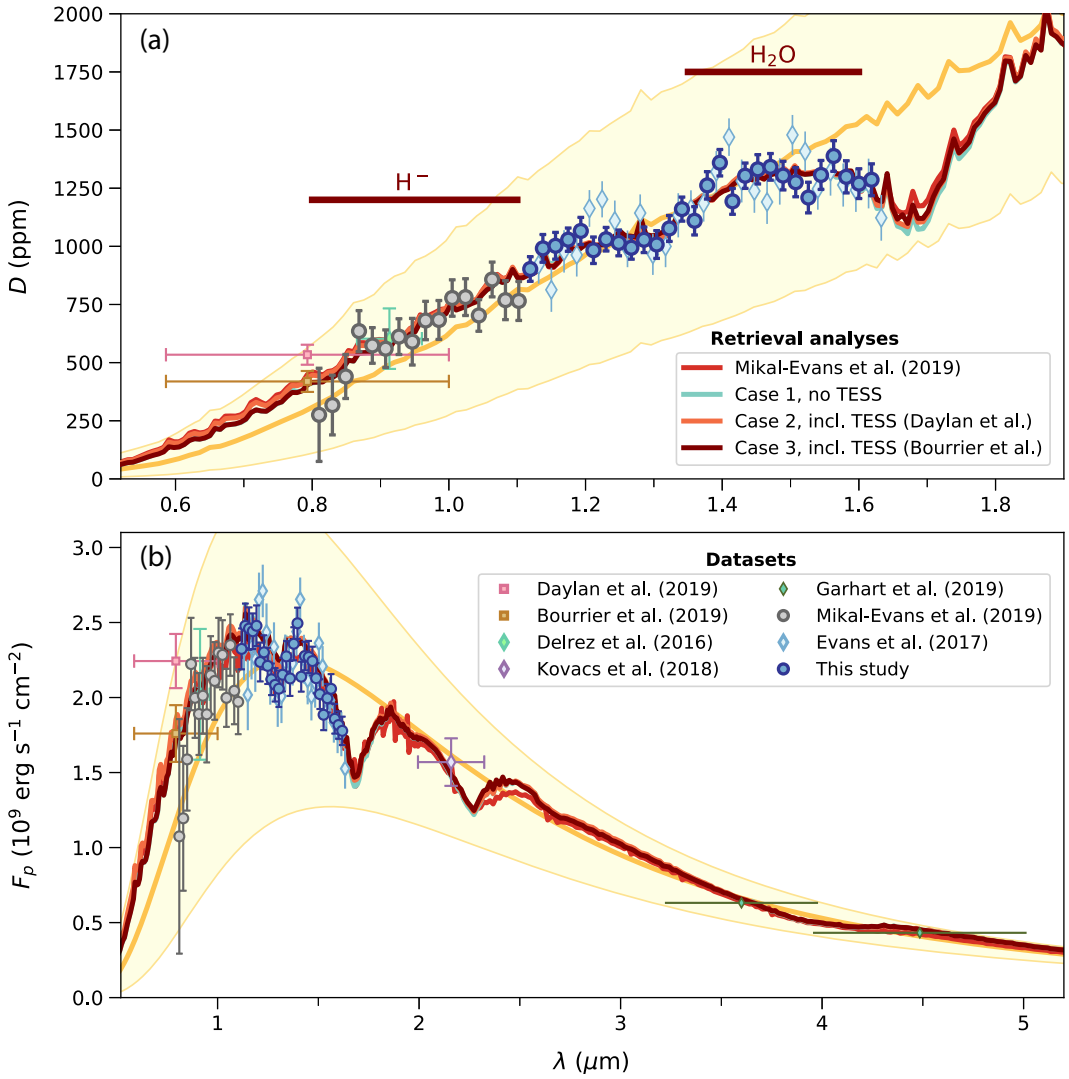

Figure 3. (a) Published eclipse depth measurements for WASP-121b across the red optical and near-infrared wavelength range covered by the *TESS* and *HST* WFC3 passbands. Note in particular the improved WFC3 G141 signal-to-noise achieved for this study with five eclipse observations, compared to the original data presented in Evans et al. (2017) for a single eclipse observation. (b) Corresponding planetary emission extending out to longer wavelengths including the *Spitzer* IRAC passbands. The errorbars for the IRAC measurements are not much larger than the marker symbols on this vertical scale. In both the panels, the dark yellow line shows the spectrum assuming that the planet radiates as a blackbody with a best-fitting temperature of 2700 K and the pale yellow envelope indicates blackbody spectra for temperatures of 2330 and 2970 K. The latter encompass a plausible range of emission under limiting assumptions for the albedo and day–night heat recirculation. As labelled in panel (a), other solid lines show best-fitting models obtained for the three retrieval analyses described in the main text, which all incorporate the updated WFC3 G141 spectrum, along with that obtained for our previous retrieval analysis published in Mikal-Evans et al. (2019). Spectral emission features due to H^- and H_2O are also labelled in panel (a).

benefit gained by observing multiple eclipses well separated in time. Furthermore, the median eclipse depth uncertainty across the spectroscopic channels has improved from 90 ppm (Evans et al. 2017) to 60 ppm, bringing the H_2O emission band into sharper focus across the ∼1.3–1.6 μm wavelength range. Despite the smaller uncertainties, the updated emission spectrum agrees with the best-fitting retrieval model presented in Mikal-Evans et al. (2019) (hereafter, ME19), reproduced in Fig. 3, which assumes equilibrium chemistry and accounts for the effects of thermal ionization and dissociation of molecules. This model has a temperature inversion, departing from a blackbody spectrum shortward of ∼1.3 μm due to H^- bound–free emission, between ∼1.3 and 1.6 μm due to H_2O emission, and within the 4.5 μm IRAC passband due to CO emission. Remarkably, with the revised WFC3 G141 spectrum, the χ^2 value has improved from 43.6 to 35.5 for 42 degrees of freedom, without any further tuning of the model. In Section 4.1 below, we describe updated retrieval analyses performed on the revised data set.

Phase curve measurements for WASP-121b made using *TESS* have also recently been reported by Bourrier et al. (2020a) (B20a) and Daylan et al. (2019) (D19), covering the 0.6–1 μm red optical wavelength range. For the planet-to-star dayside emission in the *TESS* passband, B20a obtain 419^{+47}_{-42} ppm, which agrees with the ME19 best-fitting retrieval model shown in Fig. 3 at the 0.4σ level. D19 report a somewhat higher dayside emission value of 534^{+42}_{-43} ppm, which is 2.3σ above the prediction of the best-fitting ME19 model. However, D19 used the same retrieval methodology as ME19 and presented a best-fitting model that is consistent with their

Table 3. Retrieval uniform prior ranges and MCMC marginalized posterior distribution medians and ±34 per cent credible intervals.

				Fitting to updated WFC3 G141[a]		
Parameter	Unit	Allowed range[b]	Mikal-Evans et al. (2019)	Case 1	Case 2	Case 3[c]
[M/H]	dex	(−2)–(2)	$1.09^{+0.57}_{-0.69}$	$1.57^{+0.30}_{-0.94}$	$1.38^{+0.42}_{-1.12}$	$1.50^{+0.31}_{-0.75}$
[C/H]	dex	(−2)–(2)	$-0.29^{+0.61}_{-0.48}$	$0.05^{+0.96}_{-1.38}$	$-0.13^{+0.85}_{-1.20}$	$0.29^{+0.70}_{-1.29}$
[O/H]	dex	(−2)–(2)	$0.18^{+0.64}_{-0.60}$	$0.78^{+0.44}_{-1.22}$	$0.56^{+0.49}_{-1.03}$	$0.71^{+0.41}_{-0.72}$
$\log_{10}(\kappa_{IR})$	dex cm^2 g^{-1}	(−5)–(0.5)	$-3.01^{+0.56}_{-0.62}$	$-2.70^{+0.22}_{-0.36}$	$-2.85^{+0.27}_{-0.55}$	$-2.61^{+0.19}_{-0.31}$
$\log_{10}(\gamma)$	dex	(−4)–(1.5)	$0.64^{+0.19}_{-0.16}$	$0.73^{+0.12}_{-0.14}$	$0.74^{+0.15}_{-0.14}$	$0.73^{+0.10}_{-0.10}$
ψ	–	0–2	$0.99^{+0.06}_{-0.09}$	$0.95^{+0.04}_{-0.05}$	$0.95^{+0.05}_{-0.06}$	$0.97^{+0.03}_{-0.03}$
Best-fitting model reduced χ^2			0.85	0.78	0.94	0.79

Notes. [a]The three cases are those described in the main text: (1) fitting to the same data set as Mikal-Evans et al. (2019), but using the updated WFC3 G141 spectrum derived in this work; (2) also including the Daylan et al. (2019) *TESS* measurement; and (3) adopting the Bourrier et al. (2020a) *TESS* measurement instead.
[b]Note that the allowed range for each of [M/H], [C/H], and [O/H] was (−1)–(2) in Mikal-Evans et al. (2019).
[c]Our favoured analysis, owing to it providing the tightest model parameter constraints and achieving the best-fitting quality (as quantified by the reduced χ^2), while including all available data.

TESS data point at the 0.7σ level. Given the posterior distributions of the ME19 and D19 retrieval analyses are consistent to within 1σ for all free parameters (i.e. [C/H], [O/H], [M/H], κ_{IR}, γ, and ψ), we deduce that the difference between the two available *TESS* analyses does not significantly affect the overall interpretation of the WASP-121b dayside spectrum. Although the best-fitting models vary slightly depending on which *TESS* analysis is adopted, the posterior distributions are affected minimally and the conclusion that the dayside atmosphere of WASP-121b has a thermal inversion remains unchanged. This is explored further in Section 4.1.

Finally, if we assume that the planet radiates as an isothermal blackbody and adopt the B20a *TESS* data point,[1] we obtain a best-fitting temperature of 2703 ± 6 K. However, the fit to the data is poor (Fig. 3) and can be ruled out at 6.6σ confidence. If instead we adopt the D19 *TESS* data point, the best-fitting temperature is indistinguishable (2704 ± 6 K) and can be ruled out at 7.6σ confidence. The updated G141 data set presented here and the *TESS* measurements recently reported in the literature therefore reinforce the conclusion that the dayside emission of WASP-121b is strongly inconsistent with an isothermal blackbody and is instead well explained by an atmosphere model including a thermal inversion.

4.1 Retrieval analyses

Using the updated WFC3 G141 emission spectrum, we repeated the retrieval analysis described in ME19 for three separate data set combinations: (Case 1) the WFC3 G102 and G141 spectrophotometry, *Spitzer* IRAC photometry (Garhart et al. 2020), and published ground-based photometry (Delrez et al. 2016; Kovács & Kovács 2019); (Case 2) the same, but also including the Daylan et al. (2019) *TESS* eclipse measurement; and (Case 3) the same again, but instead adopting the Bourrier et al. (2020a) *TESS* measurement. Our retrieval framework utilizes the ATMO code of Tremblin et al. (2015), which has been further developed by Tremblin et al. (2016, 2017a, b, 2019), Amundsen et al. (2014), Drummond et al. (2016), Goyal et al. (2018, 2019), and Phillips et al. (2020), and employed in numerous other exoplanet retrieval analyses (e.g. Evans et al. 2017, 2018; Wakeford et al. 2017, 2018; Alam et al. 2018; Nikolov et al. 2018b, a; Carter et al. 2020). As in ME19, the free parameters of our model were: the carbon abundance ([C/H]); oxygen abundance ([O/H]); metallicity of all other heavy elements ([M/H]); infrared opacity (κ_{IR}); ratio of the visible to infrared opacity ($\gamma = \kappa_V/\kappa_{IR}$); and an irradiation efficiency factor (ψ). For additional details, refer to ME19.

The best-fitting spectra obtained for each retrieval are all in close agreement and plotted in Fig. 3. The marginalized posterior distributions for the model parameters are reported in Table 3 and shown in Fig. 4. All three retrievals performed using the updated WFC3 G141 spectrum improve the constraints on the parameters controlling the pressure-temperature (PT) profile (i.e. κ_{IR}, γ, and ψ). This can be appreciated in Fig. 5, which shows the PT profile distributions obtained for each retrieval analysis, along with the normalized contribution functions of the *TESS*, *HST*, and *Spitzer* passbands.

For the parameters controlling elemental abundances (i.e. [M/H], [C/H], and [O/H]), the results are also consistent with those reported in ME19. However, in this work, we allowed the abundances to vary between −2 and 2 dex, whereas the lower bounds were set to −1 dex in ME19. Consequently, the posterior distributions we obtain here for [M/H], [C/H], and [O/H] are typically broader than those reported in ME19. Despite this, for [M/H] and [O/H] the upper bounds are better constrained for each of the three retrievals performed in this work (Table 3). This is likely due to two main reasons. First, the WFC3 G141 spectrum is dominated by an H_2O band, but does not encompass any strong bands due to carbon-based species. Hence, improving the precision on the WFC3 G141 spectrum results in a better constraint for [O/H] while providing little additional information for [C/H]. Secondly, the better constrained H_2O abundance provides a reference level for the H^- bound–free continuum, which spans the WFC3 G102 passband and short-wavelength half of the WFC3 G141 passband [e.g. see fig. 1 of Arcangeli et al. (2018) and fig. 12 of (ME19)]. This serves to calibrate the H^- abundance, and hence the free electron abundance of the atmosphere, which is closely linked to [M/H] via ionized heavy elements such as Na and K.

We also note that our retrieval results are overall consistent with those presented in D19. This is to be expected, as identical retrieval methodologies were employed in both studies and the same data were analysed, with the exception of the updated WFC3 G141

[1]Note that for these calculations, we use a planet-to-star radius ratio of $R_p/R_\star = 0.1205$, approximately corresponding to the lowest point of the Evans et al. (2018) transmission spectrum.

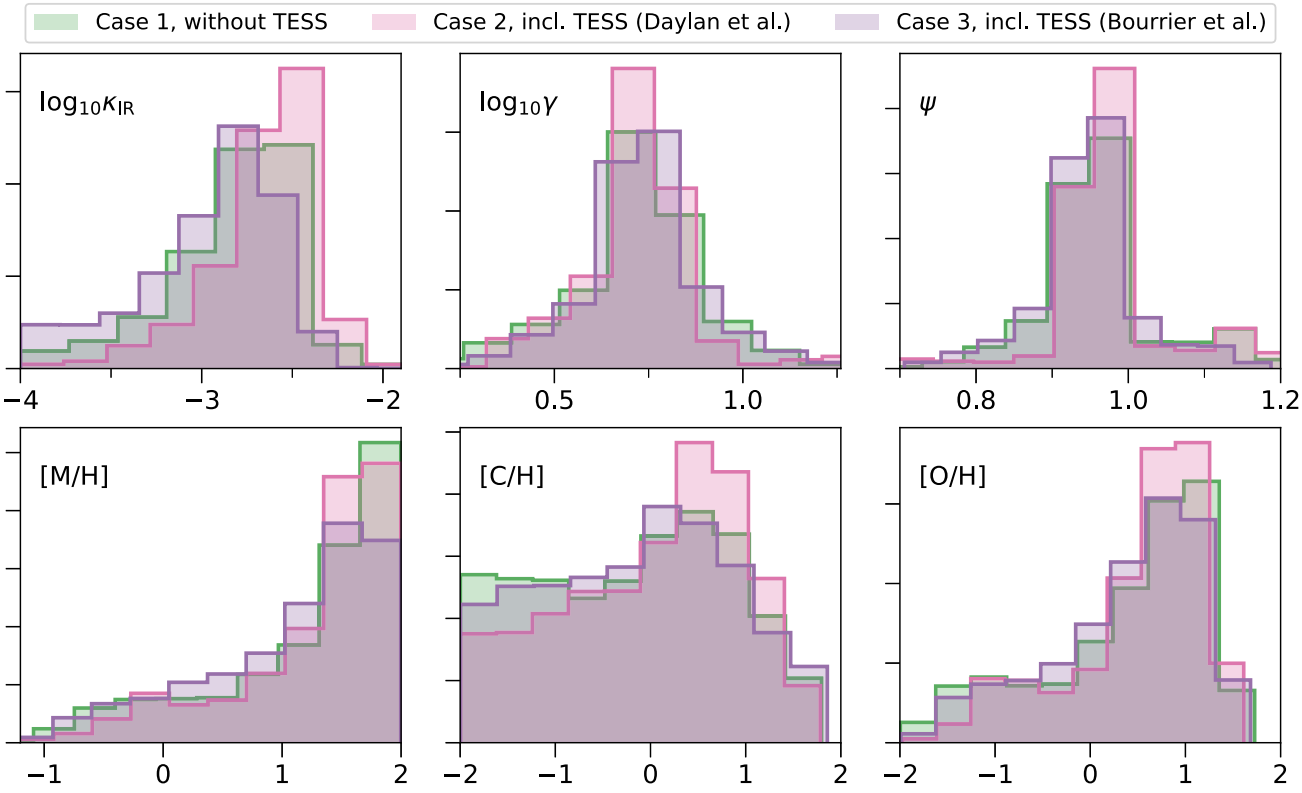

Figure 4. Marginalized posterior distributions for the retrieval analyses described in the main text, which all adopt the updated WFC3 G141 emission spectrum presented in this work. Good agreement is obtained for all three cases. Note that the lower bound on [C/H] remains poorly constrained, as the available data do not spectrally resolve any carbon-bearing species. The upper bound of [M/H] also remains unconstrained, due to the imposition of a hard limit of <2 dex in the retrievals reported here, but future analyses should consider relaxing this assumption.

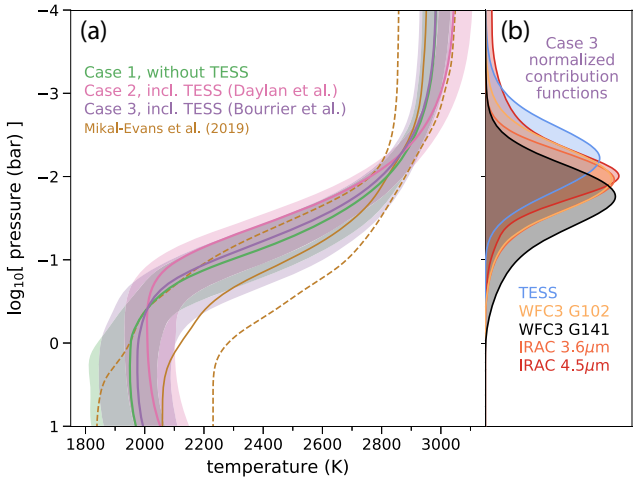

Figure 5. (a) Retrieved PT profiles obtained for the three retrieval cases described in the main text. Solid lines indicate the median temperature at each pressure level across all PT profiles sampled by the MCMC analyses. Shaded regions indicate the temperature ranges at each pressure level encompassing ±34 per cent of MCMC samples about the median. The corresponding PT distribution obtained in Mikal-Evans et al. (2019) is also shown for comparison. (b) Normalized contribution functions corresponding to the best-fitting model shown in Fig. 3 for the Case 3 retrieval (i.e. including all latest available data and adopting the Bourrier et al. 2020a *TESS* data point).

spectrum adopted in this work. Additionally, our retrieval analyses are complementary to that presented in B20a. In particular, the B20a study allowed chemical abundances to vary freely, whereas our retrieval analyses enforced chemical equilibrium while allowing [M/H], [C/H], and [O/H] to vary. Despite these differences, visual inspection suggests that the retrieved PT profile of B20a is in good agreement with those shown in Fig. 5, increasing from ∼2200 K at 100 mbar to ∼2900 K at 10 mbar.

5 CONCLUSION

We presented four new secondary eclipse observations of WASP-121b made with *HST*/WFC3 using the G141 grism, adding to the single eclipse observation previously reported in Evans et al. (2017). The additional data significantly increase the signal-to-noise of the measured dayside emission spectrum, with the median eclipse depth uncertainty reducing from 90 to 60 ppm in 28 spectroscopic channels spanning the 1.12–1.64 μm wavelength range. The updated spectrum is in excellent agreement with the best-fitting model presented in ME19, exhibiting an H_2O emission feature in the G141 passband, muted in amplitude due to thermal dissociation. Retrieval analyses performed using the updated WFC3 G141 spectrum allow tighter constraints to be placed on the PT profile in particular. These results reinforce the conclusion of previous studies (Evans et al. 2017; Bourrier et al. 2020a; Daylan et al. 2019; Mikal-Evans et al. 2019) that the dayside hemisphere of WASP-121b has a thermal inversion.

ACKNOWLEDGEMENTS

The authors are grateful to the anonymous referee for their constructive feedback. Based on observations made with the National Aeronautics and Space Administration/European Space Agency (NASA/ESA) *HST*, obtained from the data archive at the Space Telescope Science Institute. STScI is operated by the Association of Universities for Research in Astronomy, Inc. under NASA contract NAS 5-26555. Support for this work was provided by NASA through grant number GO-15134 from the Space Telescope Science Institute, which is operated by AURA, Inc., under NASA contract NAS 5-26555.

REFERENCES

Alam M. K. et al., 2018, AJ, 156, 298
Amundsen D. S., Baraffe I., Tremblin P., Manners J., Hayek W., Mayne N. J., Acreman D. M., 2014, A&A, 564, A59
Arcangeli J. et al., 2018, ApJ, 855, L30
Bourrier V. et al., 2020a, A&A, 637, A36
Bourrier V. et al., 2020b, A&A, 635, A205
Cabot S. H. C., Madhusudhan N., Welbanks L., Piette A., Gandhi S., 2020, MNRAS, 494, 363
Carter A. L. et al., 2020, MNRAS, 494, 5449
Daylan T. et al., 2019, preprint (arXiv:1909.03000)
Delrez L. et al., 2016, MNRAS, 458, 4025
Drummond B., Tremblin P., Baraffe I., Amundsen D. S., Mayne N. J., Venot O., Goyal J., 2016, A&A, 594, A69
Evans T. M. et al., 2016, ApJ, 822, L4
Evans T. M. et al., 2017, Nature, 548, 58
Evans T. M. et al., 2018, AJ, 156, 283
Fortney J. J., Lodders K., Marley M. S., Freedman R. S., 2008, ApJ, 678, 1419
Gandhi S., Madhusudhan N., 2019, MNRAS, 485, 5817
Garhart E. et al., 2020, AJ, 159, 137
Gibson N. P. et al., 2020, MNRAS, 493, 2215
Goyal J. M. et al., 2018, MNRAS, 474, 5158
Goyal J. M., Wakeford H. R., Mayne N. J., Lewis N. K., Drummond B., Sing D. K., 2019, MNRAS, 482, 4503
Hubeny I., Burrows A., Sudarsky D., 2003, ApJ, 594, 1011
Knutson H. A., Benneke B., Deming D., Homeier D., 2014, Nature, 505, 66
Kovács G., Kovács T., 2019, A&A, 625, A80
Kreidberg L. et al., 2014, Nature, 505, 69
Lothringer J. D., Barman T., Koskinen T., 2018, ApJ, 866, 27
Merritt S. R. et al., 2020, A&A, 636, A117
Mikal-Evans T. et al., 2019, MNRAS, 488, 2222
Nikolov N. et al., 2018a, MNRAS, 474, 1705
Nikolov N. et al., 2018b, Nature, 557, 526
Parmentier V. et al., 2018, A&A, 617, A110
Phillips M. W. et al., 2020, A&A, 637, A38
Sing D. K. et al., 2019, AJ, 158, 91
Stevenson K. B., Fowler J., 2019, Technical Report, Analyzing Eight Years of Transiting Exoplanet Observations Using WFC3's Spatial Scan Monitor, Space Telescope Science Institute (STScI), Baltimore, MD
Tremblin P., Amundsen D. S., Mourier P., Baraffe I., Chabrier G., Drummond B., Homeier D., Venot O., 2015, ApJ, 804, L17
Tremblin P., Amundsen D. S., Chabrier G., Baraffe I., Drummond B., Hinkley S., Mourier P., Venot O., 2016, ApJ, 817, L19
Tremblin P. et al., 2017a, ApJ, 841, 30
Tremblin P. et al., 2017b, ApJ, 850, 46
Tremblin P. et al., 2019, ApJ, 876, 144
Wakeford H. R. et al., 2017, Science, 356, 628
Wakeford H. R. et al., 2018, AJ, 155, 29

This paper has been typeset from a TEX/LATEX file prepared by the author.